

# SoraNav: Adaptive UAV Task-Centric Navigation via Zeroshot VLM Reasoning

Hongyu Song, Rishabh Dev Yadav, Cheng Guo, and Wei Pan

**Abstract**—Interpreting visual observations and natural language instructions for complex task execution remains a key challenge in robotics and AI. Despite recent advances, executing language-driven navigation remains difficult, particularly for UAVs in small-scale 3D environments. Existing Vision-Language Navigation (VLN) approaches are predominantly designed for ground robots and cannot generalize to aerial tasks that require full 3D spatial reasoning. The emergence of large Vision-Language Models (VLMs) such as GPT and Claude enables zero-shot semantic reasoning from visual and textual inputs, but these models lack spatial grounding and are not directly applicable to navigation. To address these limitations, SoraNav is introduced, an adaptive Unmanned Aerial Vehicle (UAV) navigation framework that integrates zero-shot VLM reasoning with geometry-aware decision making. 1) Geometric priors are incorporated into image annotations to constrain the VLM action space and enhance decision quality; 2) A hybrid switching strategy leverages navigation history to alternate between VLM reasoning and geometry-based exploration, mitigating dead-ends and redundant revisits; 3) A PX4-based hardware-software platform, comprising both a digital twin and physical micro-UAV, enables reproducible evaluation. Experimental results show that in 2.5D scenarios, our method improves Success Rate (SR) by 25.7% and Success weighted by Path Length (SPL) by 17%. In 3D scenarios, it improves SR by 29.5% and SPL by 18.5% relative to the baseline.

**Index Terms**—Search and Rescue Robots; Vision-Based Navigation; Autonomous Navigation

## I. INTRODUCTION

Interpreting visual observations and natural language instructions for complex task execution remains a key challenge in robotics. In navigation tasks, this requires reasoning over 3D environments [1] while aligning actions with high-level task descriptions [2]. Such embodied intelligence enables applications in industrial monitoring [3], assistive navigation [4], and search-and-rescue [5]. For instance, in a construction site, a robot may be instructed to “navigate to the electronic box in the storage room.” Classical approaches rely on full exploration of the environment [6] and continuous object detection. However, UAVs operating under tight constraints (e.g., endurance, sensing) require task-aware decisions from language without complete scene exploration.

Despite recent advances, executing complex navigation tasks from natural language remains difficult, especially for UAVs operating in small-scale environments. Existing methods fall into three categories: classical, end-to-end learning, and modular approaches. Classical methods, such as 3D reconstruction and occupancy-based exploration [7], [8], operate

The authors are with the Department of Computer Science, The University of Manchester, United Kingdom (emails: {hongyu.song-3, rishabh.yadav, cheng.guo-5}@postgrad.manchester.ac.uk; wei.pan@manchester.ac.uk).

at the voxel level and build detailed geometric maps, but lack support for language-driven tasks. End-to-end learning directly maps visual input to control actions via reinforcement or imitation learning [9], [10], but suffers from high training cost, poor generalization, and weak sim-to-real transfer. Modular pipelines [11], [12] combine perception, reasoning, and control modules, and can integrate VLMs for grounding semantic goals. However, they still require robust language-scene alignment and additional object detectors, increasing on-board computational demand. Moreover, their decision-making relies on heuristic visual-language alignment or exploratory behaviors, rather than structured reasoning. These limitations hinder their ability to support instruction-driven 3D navigation in unstructured environments.

Existing VLN research has predominantly focused on ground robots [9], [10], constraining trajectories to 2.5D and limiting exploitation of full 3D spatial structure. As a result, methods developed in simulators such as Habitat cannot generalize to UAVs, and fail in tasks like reaching elevated targets without stairs. Prior UAV-VLN studies [13] mainly address long-range navigation from high-altitude views, which suits city-scale monitoring but not small-scale industrial or domestic environments such as factory floors or small parks.

The emergence of large VLMs, such as GPT [14] and Claude [15], has enabled zero-shot semantic reasoning based on visual and textual inputs, opening new opportunities for VLN and scene understanding. This makes it feasible to pursue **Zero-shot VLM-guided Task-Centric Navigation (ZSVTN)**: a paradigm in which a robot incrementally navigates to a goal described by natural language and visual context, without task-specific training or dense semantic priors, using only the output of a pre-trained VLM. However, the general-purpose VLMs are not designed for navigation as they lack spatial grounding, generate ambiguous outputs, and cannot guarantee geometric feasibility. These limitations motivate a hybrid framework that couples VLM reasoning with geometry-aware decision-making for robust 3D UAV navigation in small-scale environments.

In this paper, we address these challenges by adopting an adaptive strategy inspired by human navigation behavior. Humans tend to move toward visible targets, explore nearby unknown areas when targets are not in sight, and avoid redundant revisits. Their decisions often rely on visual cues (e.g., doorways or intersections) as implicit waypoints, rather than explicit coordinates. Motivated by these insights, we present **SoraNav**, an adaptive navigation framework for small-scale UAVs that fuses zero-shot VLM reasoning with geometry-consistent decision making, as illustrated in Figure 1. Our

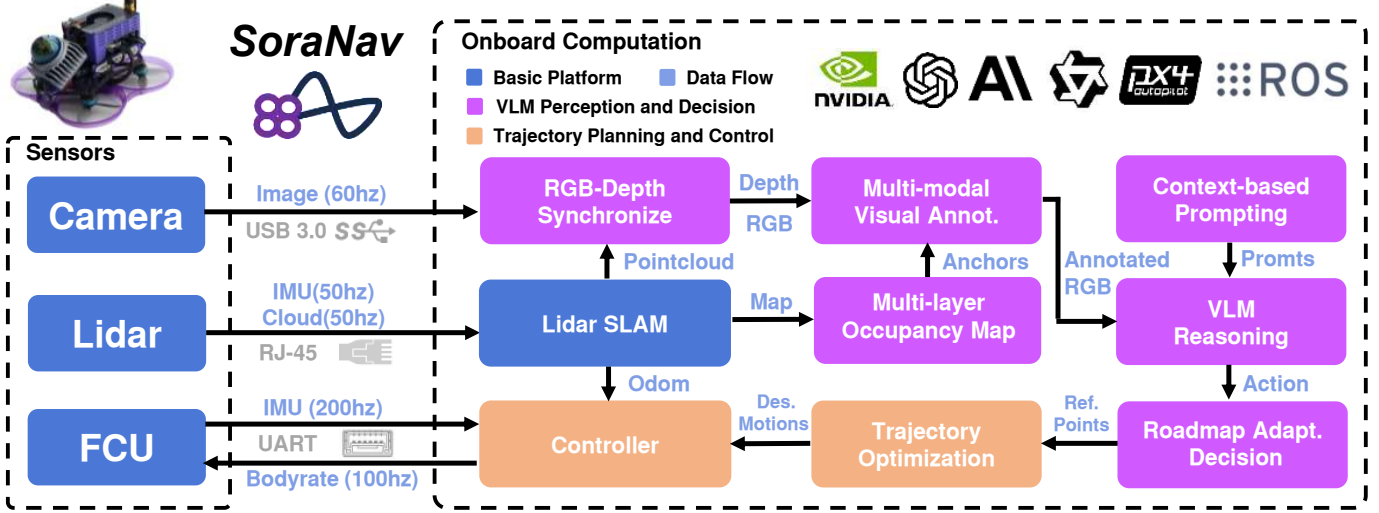


Fig. 1: Illustration of the System Overview and Data Flow.

contributions are summarized as follows:

- **Multi-modal Visual Annotation:** Image annotations enriched with geometric priors help define a clearer action space, improving the effectiveness of VLM-guided decisions.
- **Adaptive Decision Making:** A hybrid switching strategy evaluates past navigation history to alternate between VLM reasoning and geometry-based exploration, avoiding dead-ends and redundant revisits.
- **Hardware–Software Platform:** A PX4-based digital twin and a real micro-UAV setup are provided for ZSVTN, to be released as open source upon acceptance.

The framework is evaluated in simulation and real-world experiments using pretrained VLMs, and comprehensive comparison and ablation studies are carried out to validate its performance.

## II. RELATED WORKS

Classical navigation methods primarily rely on Simultaneous Localization and Mapping (SLAM) and either predefined goal positions or frontier-based exploration to achieve full-map coverage. For instance, [7] maintains an incremental frontier structure for efficient exploration, and [16] combines travel time with information gain for cross-floor planning in unknown environments. Semantic extensions such as [17] integrate global labeling into 3D mapping but remain geometry-centric. While effective for coverage, these approaches lack the capability to interpret goals expressed in semantic or natural-language form.

End-to-end learning directly maps visual observations to control actions, implicitly fusing visual and semantic information. [9] augments training environments by inserting target objects to improve task diversity and generalization. [10] leverages large-scale human demonstrations to train agents for object-goal search in real-world scenes. [18] introduces a hierarchical semantic memory to reduce redundant exploration and shorten navigation paths. While these methods learn semantic

grounding implicitly, they require extensive supervision, are prone to overfitting, and generalize poorly across domains.

Modular approaches bridge classical and end-to-end paradigms by integrating learning-based perception with traditional navigation modules. [11] employs dual vision-language models for language grounding and waypoint selection. [12], [19] combine object detection via foundation models with frontier-based exploration to enable goal-directed behavior. While more deployable than classical or end-to-end methods, modular approaches still rely on multiple vision or VLM components, handcrafted strategies, and predefined goal labels. Collectively, existing paradigms struggle to support instruction-driven 3D navigation in unstructured environments.

Most existing VLN studies target ground navigation and lack applicability to UAVs or real-world deployment. Works such as [10], [9], [12] are built in ground-robot simulators like Habitat, which assume 2.5D motion and ground-centric perception. These methods are difficult to transfer to aerial platforms due to differences in dynamics, field-of-view constraints, and altitude control. Recent UAV-VLN efforts [13], [20] explore large-scale urban scenes using high-fidelity simulators, but adopt loose success thresholds (e.g., 20 meters). Such settings are unsuitable for small-scale, cluttered environments e.g., industrial inspection or indoor search, where precise semantic understanding and short-horizon reasoning are critical. This gap motivates the need for a UAV-VLN framework tailored to compact 3D spaces with real-time, instruction-driven navigation.

Large VLMs possess rich common sense knowledge, enabling them to perform scene understanding, object recognition, and even reasoning over navigation tasks, which makes ZSVTN feasible. In 2D navigation, [21] [22] propose to annotate images with candidate targets and let the VLM select the most relevant one; experiments show that their annotated representations guide decision-making more effectively than raw images. In 3D navigation, [13] [20] utilize VLMs to infer spatial waypoints as navigation targets in real-world UAV scenarios. However, due to hallucinations [23] and a

lack of explicit spatial scale awareness, VLMs can generate unsafe or unreasonable commands when reasoning from visual inputs alone. This highlights the need for proper instruction grounding and adaptive decision mechanisms that can provide fallback plans during navigation.

### III. PROBLEM DEFINITION

We consider the problem of **ZSVTN** in unknown environments, where a UAV progressively explores and reaches a target described only by humans as natural language instructions, leveraging no prior knowledge of similar objects or other semantic annotations. At each step, a pre-trained VLM receives the sensory observation and outputs a local navigation decision, which is translated into an executable local goal by the low-level planner-controller.

We formulate the ZSVTN as a *Markov Decision Process (MDP)*  $\langle \mathcal{S}, \mathcal{A}, \mathcal{T}, \mathcal{P} \rangle$ :

- $s_k = ({}^G p_k, o_k, \mathcal{V}_{1:k-1}^{\text{rm}}) \in \mathcal{S}$  is the state at step  $k$ , where  ${}^G p_k$  is the drone pose,  $o_k$  is the perceptual observation (e.g., RGB image, occupancy map), and  $\mathcal{V}_{1:k-1}^{\text{rm}}$  denotes the set of all previously visited roadmap vertices.
- $a_k \in \mathcal{A}$  is the action determined by the high-level policy, represented as a hypergraph vertex, which can be mapped to the target pose  ${}^G p_k^{\text{goal}}$ .
- $\mathcal{T} : \mathcal{S} \times \mathcal{A} \rightarrow \mathcal{S}$  is the transition function describing the evolution of the drone state under the low-level planner-controller.
- $\mathcal{P}$  is the context-based prompt of the navigation task.

In our approach, the high-level policy  $\pi(a_k \mid s_k, \mathcal{P})$  is directly realized by the VLM with a adaptive decision making process, rather than through optimization.

### IV. MULTI-MODAL VISUAL ANNOTATION

Since a VLM cannot directly infer geometric scales or frontier-related information from raw RGB images, we propose a **Multi-modal Visual Annotation (MVA)** scheme to encode such information. The observation is  $o_k^{\text{mva}} = (i_k^{\text{mva}}, m_k^h)$ , where  $i_k^{\text{mva}}$  is the original RGB frame  $i_k$  annotated by spatial guiding anchors, and  $m_k^h$  is the 2D frontier map corresponding to the current flight altitude layer  $h$ . These annotations reveal traversability, unknown-space layout, and vertical navigability directly from a first-person view. An illustration of the anchors and visual annotation is shown in Figure 2.

#### A. Depth Alignment

To ensure that the anchors selected by the VLM from the RGB image correspond to precise spatial locations, we align LiDAR point clouds with RGB frames via extrinsic–intrinsic projection, thereby combining geometric accuracy with semantic perception. Let  ${}^B T_C$  and  ${}^B T_{\text{lidar}}$  denote the camera and LiDAR poses in the body frame  $B$ , and  ${}^G T_B$  the body pose in the global frame  $G$ . A LiDAR point  ${}^G p_{\text{lidar}}$  is transformed into the camera frame  $C$  as

$${}^C p_{\text{lidar}} = ({}^B T_C)^{-1} ({}^G T_B)^{-1} {}^G p_{\text{lidar}}. \quad (1)$$

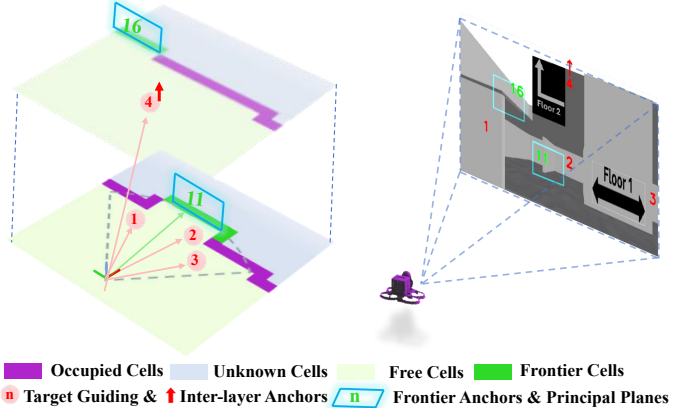


Fig. 2: Illustration of Anchors and Visual Annotations.

Then, the 3D point  ${}^C p_{\text{lidar}} = ({}^C X, {}^C Y, {}^C Z)$  is projected onto the image plane using the intrinsic matrix  $K$  [24]:

$$u = \frac{f_x {}^C X}{{}^C Z} + c_x, \quad v = \frac{f_y {}^C Y}{{}^C Z} + c_y, \quad (2)$$

with the depth value

$$D(u, v) = {}^C Z. \quad (3)$$

Leveraging the high precision and low noise of the Mid-360, we employ a sliding-window integration to accumulate LiDAR point clouds and maintain a real-time aligned depth map.

#### B. Multi-layer Occupancy Map

To reduce annotation clutter and enable the VLM to interpret traversable regions across different heights, we encode the 3D scene as multi-layer 2D occupancy map  $\mathcal{M} = \{m^h \mid h \in \mathcal{H}\}$  [14], where  $\mathcal{H}$  denotes the set of all height layers. Each cell is labeled as free, occupied, or unknown via raycasting. Frontiers are incrementally updated following [7], and for simplicity only the main plane and view point of each frontier in the 2D height layers are considered.

#### C. Spatial Guiding Anchors

1) *Frontier Anchors*: The height of each frontier plane is determined by the spacing between adjacent height layers. For a frontier cluster  $\mathcal{F}_c$  in a 2D occupancy map, we compute its principal axis  $\mathbf{d}_c$  and define the planar length as  $\ell_c$ . If  $\ell_c > \ell_{\text{max}}$ , the cluster is partitioned into smaller planar segments, where  $\ell_{\text{max}}$  denotes the maximum allowed length for a frontier cluster. Each frontier plane is approximated by four corner points  $\mathbf{w}_i = ({}^G X_i, {}^G Y_i, {}^G Z_i)$ ,  $i = 1, \dots, 4$  in the global frame. They are transformed into the camera frame and projected onto the image plane. Specifically, the FOV  $\mathcal{F}({}^G p_k)$  is the spherical cap centered at  ${}^G p_k$  with radius  $d_{\text{max}}$  and half-angle  $\theta_{\text{max}}$ . If all projected corner points are inside the camera field of view, the corresponding frontier plane, defined by connecting its four corner points, is displayed on the RGB frame as an annotation. The contours of the frontier planes are shown in cyan, and their indices are labeled in green, as illustrated in Figure 2.

2) *Target Anchors*: Let  $\mathcal{F}_{\text{obs}}(G p_k) \subset \mathcal{F}(G p_k)$  denote the subset of frontiers that are geometrically located within  $\mathcal{F}(G p_k)$ . The *observable frontier count* is  $n_{\text{obs}}(G p_k)$ . Given a nominal angular span  $[\varphi_{\text{L}}, \varphi_{\text{R}}]$  (left/right sector bounds), we define an *adaptive sampling cardinality*:

$$m_{\varphi} = \begin{cases} m_{\text{max}}, & \text{if } n_{\text{obs}}(G p_k) < \tau_{\text{obs}}, \\ m_{\text{nom}}, & \text{otherwise.} \end{cases} \quad (4)$$

where  $\tau_{\text{obs}}$  is the scarcity threshold,  $m_{\text{nom}}$  and  $m_{\text{max}}$  denote the nominal and maximum numbers of target directions. The discrete yaw set for target generation is then obtained via uniform discretization:

$$\Phi(G p_k) \triangleq \left\{ \varphi_{\text{L}} - \frac{l-1}{m_{\varphi}-1}(\varphi_{\text{L}} - \varphi_{\text{R}}) \mid l \in \{1, \dots, m_{\varphi}\} \right\}, \quad (5)$$

For each  $\varphi \in \Phi(G p_k)$ , we cast a search ray  $\mathbf{r}(\varphi)$  from the sensor origin within the current layer map  $m_k^h$ , and we select the farthest candidate point along direction  $\varphi$  that is line-of-sight (LOS) reachable and maintains a minimum clearance distance  $r_{\text{clr}}$  from all occupied or unknown cells.

3) *Inter-Layer Anchors*: During 3D navigation, the blind zones above and below the UAV increase the risk during altitude adjustments. To mitigate this, we introduce Inter-Layer Anchors, which are activated when collision-free navigation paths exist between adjacent height layers (e.g., they remain inactive if a ceiling is present above the UAV).

## V. ADAPTIVE DECISION MAKING & TRAJECTORY PLANNING

To enable effective navigation under VLM reasoning, we propose an **Adaptive Decision Making (ADM)** mechanism. Based on the MVA module, multi-modal prompting is first performed to obtain semantic proposals from the VLM. The prompting results are then validated by the Roadmap Adaptive Decision process, which determines whether to follow the VLM's suggestion or navigate toward nearby unexplored regions for re-prompting. The final decision is converted into waypoints for trajectory generation and subsequent control commands. An overview of the ADM pipeline is illustrated in Figure 3.

### A. Multi-modal Prompting

1) *Context-Based Prompt*: Inspired by [25], we design a structured context-based task prompt for querying a VLM. The prompt consists of four essential components:

$$\mathcal{P} = \{RG, OI, IG, BO, OS\}.$$

- **RG (Role and Goal)**: Defines the operational role and mission objective, describing the scene and specifying the goal.
- **OI (Observation Input)**: The components of  $o_k^{\text{mva}}$  are specified, and the VLM is instructed on their interpretation.
- **IG (Important Guidelines)**: Encodes task-specific constraints that guide how the VLM interprets observations and prioritizes MVA.

- **BO (Behavior Options)**: Defines permissible actions: selecting a target  $g_k$  or a yaw adjustment  $\Delta\psi_k$ .
- **OS (Output Schema)**: Specifies the structured output format, ensuring compatibility with downstream processing.

This structured approach helps the VLM receive a clear and organized description of the environment, sensor data, available actions, and output format.

2) *Prompting the VLM*: Finally, we query the large VLM with the multi-modal observation  $o_k^{\text{mva}}$  under the structured prompt  $\mathcal{P}$  to infer a high-dimensional action:

$$(o_k^{\text{intp}}, a_{\text{ref}}, c_{\text{det}}) = \text{VLM}(o_k^{\text{mva}} \mid \mathcal{P}) \quad (6)$$

where  $o_k^{\text{intp}}$  is the VLM's semantic interpretation of the observation,  $a_{\text{ref}}$  is an action complying with the output schema *OS* and is used for subsequent adaptive decision-making. The scalar confidence  $c_{\text{det}} \in (0, 1)$  reflects the VLM's internal estimate of object existence and is numerically stabilized by clipping,  $\tilde{c}_{\text{det}} = \text{clip}(c_{\text{det}}, \varepsilon, 1 - \varepsilon)$ .

### B. Roadmap Adaptive Decision

1) *Hypergraph Formulation*: We define the **hypergraph space**  $\mathcal{H} = (\mathcal{V}^{\text{rm}}, \mathcal{E})$ , where  $\mathcal{V}^{\text{rm}}$  is the set of *Roadmap Vertices* that encode full decision states of MDP, and  $\mathcal{E}$  is the set of decision-driven hyperedges. Each hyperedge  $e_k \in \mathcal{E}$  encapsulates  $k$ -th step in MDP, linking the current Roadmap Vertex  $v_k^{\text{rm}}$  to its candidates originating from different sources:

$$e_k = \{v_{k-1}^{\text{rm}}, v_k^{\text{rm}}, \{v_k^{\text{vlm}}, v_k^{\text{geo}}\}\} \quad (7)$$

The elements are specified as follows:

- $v_k^{\text{rm}} \in \mathcal{V}^{\text{rm}}$  is the roadmap vertex at decision step  $k$ ,
- $v_k^{\text{vlm}} \in \mathcal{C}_k^{\text{vlm}}$  is the candidate vertex proposed by the VLM using MVA,
- $v_k^{\text{geo}} \in \mathcal{C}_k^{\text{geo}}$  is the candidate vertex selected by the geometry-based strategy [26],
- $v_k^{\text{sw}} \in \mathcal{C}_k^{\text{sw}}$  is the candidate representing an inter-layer transition.

Each vertex  $v$  contains its global position  $G p$ , from which the yaw angle  $\psi$  can be directly derived.

2) *Candidate Validation*: For each step  $k$ , the exploration value of a VLM-proposed candidate  $v_k^{\text{vlm}}$  is quantified by comparing its raycast observations with the historical FOV coverage.

Instead of all historical vertices, we only consider the  $K$  nearest visited Roadmap Vertices to  $v_k^{\text{vlm}}$ , denoted by  $\mathcal{N}_K(v_k^{\text{vlm}}) \subset \mathcal{V}_{1:k-1}^{\text{rm}}$ . The local past coverage is

$$\mathcal{F}_{\text{past}}(v_k^{\text{vlm}}) \triangleq \bigcup_{v_j \in \mathcal{N}_K(v_k^{\text{vlm}})} \mathcal{F}(v_j), \quad (8)$$

Let  $\text{Occ} : m^h \rightarrow \{-1, 0, 1\}$  denote the occupancy of the current layer map, where  $-1$ ,  $0$ , and  $1$  indicate unknown, free, and occupied cells, respectively. For each azimuth angle  $\theta_m \in \mathcal{F}(G p_k)$ , define the discrete ray as

$$\mathcal{R}(v_i^{\text{vlm}}, \theta_m) \triangleq \{g_{\ell} \in \mathbb{G} \mid \ell \in \mathbb{N}^+\}, \quad (9)$$

where  $g_{\ell}$  denotes a grid cell and  $\mathbb{G}$  is the set of all grid cells in  $m^h$ . The discrete ray is the ordered sequence of

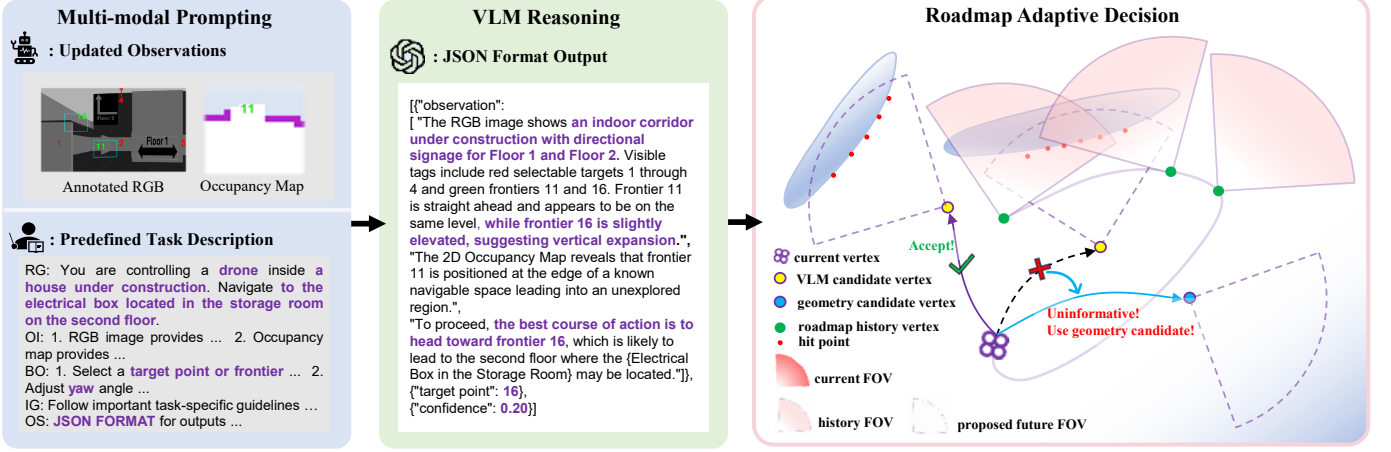


**Fig. 3: Pipeline of Adaptive Decision Making.** The pipeline illustrates how multi-modal prompting is employed to guide the Large VLM in reasoning and decision generation. Example reasoning outputs from the VLM are shown for context. A roadmap hypergraph is then used to validate the effectiveness of VLM decisions, enabling a transition from *uninformative* VLM decisions to *geometric* strategies.

grid cells in  $m^h$  generated by the Bresenham integer line algorithm [27] from the viewpoint  $\mathbf{p}_k$  along direction  $\mathbf{d}_m = [\cos \theta_m, \sin \theta_m]^\top$ . The *hit point* of the  $m$ -th ray is then

$$h_k^m = \text{center}(g_{\ell^*}), \quad \ell^* = \min\{\ell \mid \text{Occ}(g_\ell) \in \{0, 1\}\}. \quad (10)$$

where  $\text{center}(\cdot)$  returns the Cartesian coordinates of the cell. The set of all hit points at step  $k$  is  $\mathcal{H}_k = \{h_k^1, \dots, h_k^{M_k}\}$ .

Let  $s_k^m \in \{0, 1\}$  denote the binary visibility indicator of  $h_k^m$ , defined as

$$s_k^m \triangleq \max_{v_j \in \mathcal{N}_K(v_k^{\text{vlm}})} \mathbb{1}(h_k^m \in \mathcal{F}(v_j)), \quad (11)$$

where  $\mathbb{1}(\cdot)$  is the indicator function that evaluates to 1 if the hit point is within the field of view of a neighboring node, and 0 otherwise.

The information gain at  $v_k^{\text{vlm}}$  is then computed as

$$G(v_k^{\text{vlm}}) \triangleq \frac{1}{M_k} \sum_{h_k^m \in \mathcal{H}_k} (1 - s_k^m), \quad (12)$$

which reflects the proportion of newly observed hit points.

To facilitate probabilistic reasoning, we map the gain to a confidence score via a logistic function:

$$P_G(v_i^{\text{vlm}}) \triangleq \sigma(\alpha(G(v_i^{\text{vlm}}) - \tau_G)), \quad (13)$$

where  $\alpha > 0$  controls the slope, and  $\tau_G$  sets the gain threshold for positive influence. This mono value serves as a *soft evidence term*. The detection-conditioned validation probability is computed via log-odds fusion:

$$P_{\text{valid}}(v_i^{\text{vlm}}) = \sigma(\text{logit}(P_G(v_i^{\text{vlm}})) + \lambda \text{logit}(\tilde{c}_{\text{det}})), \quad (14)$$

where  $\sigma(x) \triangleq (1 + e^{-x})^{-1}$  is the logistic mapping converting log-odds to probability, and  $\text{logit}(p) \triangleq \log \frac{p}{1-p}$  maps a probability to its log-odds representation. The coefficient  $\lambda > 0$  controls the relative influence of the detection confidence term with respect to the geometric gain term. This formulation follows the log-odds fusion principle [28], where independent evidence sources (geometric gain and detection confidence)

are combined additively in the log-odds domain and then converted back to a probability via the logistic function. By combining both terms in the log-odds domain, the system filters out uninformative candidate vertices.

The target goal pose  ${}^G p_k^{\text{goal}}$  is computed from the selected anchor  $a_k$  as

$${}^G p_k^{\text{goal}} = \mathcal{P}(a_k), \quad a_k = \begin{cases} v_k^{\text{vlm}}, & \text{if } P_{\text{valid}}(v_k^{\text{vlm}}) > \tau_{\text{valid}}, \\ v_k^{\text{geo}}, & \text{otherwise.} \end{cases} \quad (15)$$

where  $\mathcal{P}(\cdot)$  denotes the mapping from the selected hypergraph node to its corresponding spatial pose, and  $\tau_{\text{valid}}$  is the validity threshold. The final yaw of  ${}^G p_{\text{goal},k}$  is determined based on detection confidence and directional deviation. When  $\tilde{c}_{\text{det}} > \tau_{\text{yaw}}$  and  $|\psi_{\text{traj}} - \psi_k| > \tau_{\Delta\psi}$ , the current yaw  $\psi_k$  is retained to ensure target visibility; otherwise, the yaw is aligned with the trajectory heading, where  $\tau_{\text{yaw}}$  is the confidence threshold for retaining yaw,  $\psi_{\text{traj}}$  is the trajectory terminal yaw, and  $\tau_{\Delta\psi}$  is the yaw deviation threshold.

### C. Trajectory Generation

To ensure that the decisions generated by the large VLM can be accurately executed, the target goal pose  ${}^G p_{\text{goal},k}$  is navigated with consideration of both efficiency and safety. Given the current pose  ${}^G p_k$ , if  ${}^G p_{\text{goal},k}$  originates from target anchors, a minimum-jerk trajectory is adopted, which is initialized by sampling along the straight line connecting  ${}^G p_k^{\text{goal}}$  and  ${}^G p_k$ . If it originates from frontier anchors, inter-layer anchors, or the geometry-based strategy, a trajectory generated following [29] is employed instead. The generated trajectory is then tracked by a controller through body-rate control.

## VI. UAV PLATFORM AND DIGITAL TWIN

To support the ZSVTN task in compact 3D environments, we designed a custom Micro Aerial Vehicle (MAV) inspired by the architecture of [30]. The platform features a compact

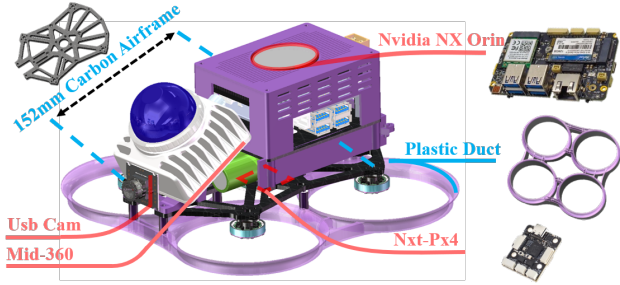


Fig. 4: Custom UAV platform designed for ZSVTN.



Fig. 5: Real-World (Left) and Simulated (Right) Flight Scenes.

152 mm diagonal span to ensure agile obstacle-aware navigation in narrow spaces, shown in Figure 4. A Mid-360 LiDAR [31] is mounted with a fixed tilt angle to enhance vertical field-of-view coverage, enabling robust real-time localization and mapping via [32], while preserving a low-profile form factor. An NVIDIA Jetson Orin NX [33] is integrated to provide sufficient onboard computational resources.

A high-fidelity digital twin of the UAV is developed using ROS [34], PX4 SITL [35], and Gazebo [36], enabling seamless transfer of the onboard software stack between simulation and the physical drone. The airframe model, defined in SDF format, replicates the real UAV’s geometry and sensor placement, and is fully compatible with PX4 firmware. For visualization, we employ a 3D model of the actual platform. Sensor simulation is performed with hardware-matched specifications, including the livox-gazebo-plugin [37] to emulate the scanning pattern of the Mid-360 LiDAR. An example of the matched real and simulated environments is illustrated in Figure 5.

## VII. RESULTS AND EALUATIONS

We designed experiments to quantitatively evaluate the contribution of each component in SoraNav and to validate its scalability from simulation to real-world deployment. Specifically, the evaluations are organized along four complementary objectives: (1) analyzing how MVA enhances spatial reasoning from single-image interpretation; (2) assessing the short- and long-horizon navigation performance enabled by ADM; (3) examining the generalizability across different VLMs; and (4) verifying the overall system performance through real-world deployment on a real UAV.

### A. Experimental Setup

*a) Evaluation Scenarios:* We evaluate the proposed framework across three complementary settings:

- **Image Spatial Reasoning:** We use 6 outdoor and 2 indoor 2.5D scenes, as well as 3 outdoor and 1 indoor 3D scenes, to assess the VLM’s ability to infer spatial relationships from single images.
- **Navigation Tasks:** We design 4 short-horizon scenarios (2 in 2.5D, 2 in 3D) and 3 long-horizon scenarios (1 in 2.5D, 2 in 3D) to test the integrated decision-making and trajectory execution over multiple steps.
- **Model Generalization and Real-World Transfer:** We evaluate generalizability across four large VLMs (GPT-4o, Sonnet 4, Qwen2.5, Gemini2.5) and deploy the full system on a physical UAV to verify robustness in real-world conditions.

*b) Evaluation Metrics:* For Image Spatial Reasoning, we report **Success Rate** (SR), **Distance to Goal** (DtG) (m), and **Normalized Residual Error** (NRE), which is

$$NRE = \frac{1}{N} \sum_{i=1}^N \left( (1 - S_i) + S_i \cdot \left( \frac{D_i}{D_{\max}} \right)^\gamma \right). \quad (16)$$

This metric captures both success and decision accuracy simultaneously, where  $S_i \in \{0, 1\}$  indicates whether the decision succeeds,  $D_i$  denotes the spatial distance between the VLM-predicted position and the ideal target location, and  $D_{\max}$  is the maximum allowable error in successful cases.

For navigation, we report SR, **Success weighted by inverse Path Length** (SPL) and DtG for all methods. SR measures whether an episode succeeds, while SPL evaluates efficiency relative to the optimal path. For navigation tasks, we additionally record the number of VLM promptings and the path length (m) required to complete the task. A navigation episode is considered successful if the UAV reaches within 3 m of the goal and the goal is visible. For short-term tasks, a maximum of 5 prompting steps is allowed, while long-term tasks allow up to 15 prompting steps. When comparing our approach across different large models, long-term tasks are restricted to a maximum of 9 prompting steps.

*c) Baselines:* Our approach is compared with four ZSVTN methods. **Spatial** follows [20], where the VLM directly de-tokenizes relative spatial positions, and thus serves as a baseline in both 2.5D and 3D environments. We further adapt three ground-robot navigation methods to aerial navigation: **NavVLM** [22], **Pivot** [21], and **CONVOI** [11]. Since these three methods do not account for altitude, they are evaluated only in 2.5D environments. NavVLM outputs collision-free points sampled at fixed angular intervals, while Pivot uniformly samples navigable waypoints; in both cases, sampled waypoints are annotated with indices on the image for the VLM to select from. CONVOI samples free cells in the occupancy grid map and requires the VLM to construct a path by sequentially connecting them.

### B. Image Spatial Reasoning

This experiment evaluates the impact of MVA on the spatial decision-making capability of vision-language models (VLMs). Each method receives the same RGB input and movement range, and must select a spatial anchor based on a natural language instruction containing both explicit and

Env & Dims	Method	Prompts ↓				Path Length ↓				DtG ↓			Obs. ↑	SR ↑	SPL↑	
		Avg	Std	Max	Min	Avg	Std	Max	Min	Avg	Std	Max				
Warehouse 2.5D	Ours	1.00	0.00	1	1	7.50	0.70	8.48	6.72	2.29	0.54	3.65	1.90	1.00	0.86	0.66
	Spatial	2.86	0.35	3	2	4.78	2.51	7.30	0.02	4.62	2.13	8.74	2.41	1.00	0.29	0.24
	Convoi	2.43	0.54	3	2	7.66	0.94	8.99	6.63	2.06	0.59	2.64	1.30	1.00	0.71	0.65
	NAVVLML	2.43	0.54	3	2	9.95	0.04	10.00	9.91	1.42	0.03	1.44	1.39	/	/	/
	PIVOT	2.57	0.54	3	2	6.95	2.05	9.48	3.75	3.53	1.84	6.86	1.56	/	/	/
Park 2.5D	Ours	1.57	0.98	3	1	9.23	3.01	15.78	7.32	2.87	0.53	3.67	2.35	1.00	0.71	0.39
	Spatial	2.86	0.35	3	2	7.94	1.16	9.90	6.04	4.35	1.31	6.18	2.63	1.00	0.14	0.07
	Convoi	2.71	0.54	3	2	13.32	7.61	28.29	6.48	4.11	2.92	9.80	1.58	0.67	0.43	0.14
	NAVVLML	3.00	0.00	3	3	6.32	2.05	10.58	5.13	5.76	0.41	6.02	4.90	/	/	/
	PIVOT	3.00	0.35	3	3	9.59	4.80	18.18	4.73	5.43	3.20	11.34	1.42	/	/	/
Warehouse 3D	Ours	2.29	1.89	5	1	12.91	8.15	26.63	7.20	4.50	3.28	9.31	2.13	0.80	0.57	0.18
	Spatial	5.00	0.00	5	5	7.36	2.10	10.94	3.77	5.96	2.71	8.34	3.05	/	/	/
Park 3D	Ours	2.14	2.07	5	1	14.13	6.14	24.67	9.36	3.59	4.32	11.85	1.27	1.00	0.71	0.56
	Spatial	4.14	0.98	5	3	11.78	2.06	14.35	9.50	2.75	0.78	3.65	1.45	0.75	0.43	0.31
Kilburn 2.5D	Ours	5.67	0.47	6	5	30.55	1.91	32.38	27.92	3.16	1.32	4.96	1.83	1.00	0.67	0.58
	Spatial	6.33	1.70	8	4	8.94	2.62	12.21	5.81	11.99	0.20	12.27	11.80	/	/	/
	Convoi	12.00	4.24	15	6	21.29	11.58	37.45	10.96	14.11	2.08	16.59	11.51	/	/	/
	NAVVLML	9.67	1.70	12	8	22.46	7.41	28.98	12.09	6.83	5.43	14.51	2.93	1.00	0.33	0.33
	PIVOT	15.00	0.00	15	15	22.40	11.22	37.99	12.09	12.41	6.40	19.00	3.74	/	/	/
Construction 3D	Ours	6.00	0.82	7	5	32.46	6.31	41.38	27.90	4.75	2.42	8.11	2.50	1.00	0.33	0.31
	Spatial	9.33	4.03	15	6	27.99	11.10	41.98	14.83	8.55	2.50	10.35	5.02	/	/	/
Snowy 3D	Ours	11.67	3.40	15	7	35.85	15.64	54.93	16.61	7.70	3.73	11.62	2.69	/	/	/
	Spatial	12.67	3.30	15	8	22.63	0.43	23.07	22.05	16.06	1.23	17.07	14.32	/	/	/

TABLE I: Short-term and Long-term Navigation. Warehouse and Park correspond to short-term tasks, while the remaining scenarios represent long-term tasks.

Env & Dims	Model	Prompts ↓				Path Length ↓				Distance to Goal ↓			Obs. ↑	SR ↑	SPL↑	
		Avg	Std	Max	Min	Avg	Std	Max	Min	Avg	Std	Max				
Kilburn 2.5D	GPT-4o	5.67	0.47	6	5	30.55	1.91	32.38	27.92	3.16	1.32	4.96	1.83	1.00	0.67	0.58
	Sonnet4	7.67	0.94	9	7	29.74	6.96	36.49	20.17	7.89	4.80	12.64	1.32	0.00	/	/
	Qwen2.5	6.00	4.24	9	0	16.59	5.59	23.94	10.39	14.78	3.17	18.97	11.30	/	/	/
	Gemini2.5	6.33	0.94	7	5	30.59	4.09	35.29	25.32	7.36	4.20	11.03	1.47	1.00	0.33	0.21
Warehouse 3D	GPT-4o	2.29	1.89	5	1	12.91	8.15	26.63	7.20	4.50	3.28	9.31	2.13	0.80	0.57	0.18
	Sonnet4	3.71	1.58	5	1	18.19	6.31	30.06	10.02	3.19	2.10	6.55	1.15	0.75	0.43	0.32
	Qwen2.5	3.43	1.68	5	1	10.01	1.78	12.43	6.67	4.84	2.84	9.66	1.34	0.33	0.14	0.13
	Gemini2.5	5.00	0.00	5	5	15.29	4.08	20.92	7.33	6.61	2.61	10.15	1.90	1.00	0.14	0.09

TABLE II: Performance Across Different VLMs.

Method	SR ↑			DtG ↓			NRE ( $\gamma = 0.5$ ) ↓					
	ours	0.83	1.62	0.65	navvilm	0.67	2.62	0.74	convoy	0.33	3.38	0.83
2.5D	spatial	0.22	6.03	0.95	pivot	0.00	6.69	1				
3D	ours	0.67	2.80	0.84	spatial	0.00	7.24	1				

TABLE III: Image Spatial Reasoning.

implicit spatial references (e.g., “*between two trees*”, “*near a shelf and a bin*”, “*right-side window on the second floor*”).

Table III shows that MVA significantly improves anchor selection accuracy, achieving the highest SR and lowest DtG/NRE across both 2.5D and 3D scenes. In 2.5D, NavVLM and CONVOI perform comparably due to structured sampling, whereas Spatial underperforms in all cases, highlighting the difficulty of inferring spatial scale directly from raw images. These results confirm that MVA provides essential geometric priors that enhance spatial grounding, particularly in cluttered

3D environments.

### C. Short-term and Long-term Navigation

Table I compares our method with baseline approaches across short- and long-term navigation tasks. In short-term scenarios, our approach consistently achieves the highest SR and SPL with the fewest VLM promptings. This advantage arises from the proposed Multi-modal Visual Annotation (MVA), which constrains the action space with geometric priors and adaptively refines candidate anchors, enabling more reliable decisions. Among the baselines, CONVOI performs competitively in 2.5D tasks by leveraging occupancy maps, while NAVVLML obtains shortest distances to the goal but suffers from low SR due to missing yaw adjustments.

In long-term tasks, only our method and NAVVLML successfully complete navigation, with our approach yielding higher SR and SPL. The longer paths arise because, when facing explored areas or infeasible decisions, our adaptive mechanism uses geometric priors to relocate the UAV for

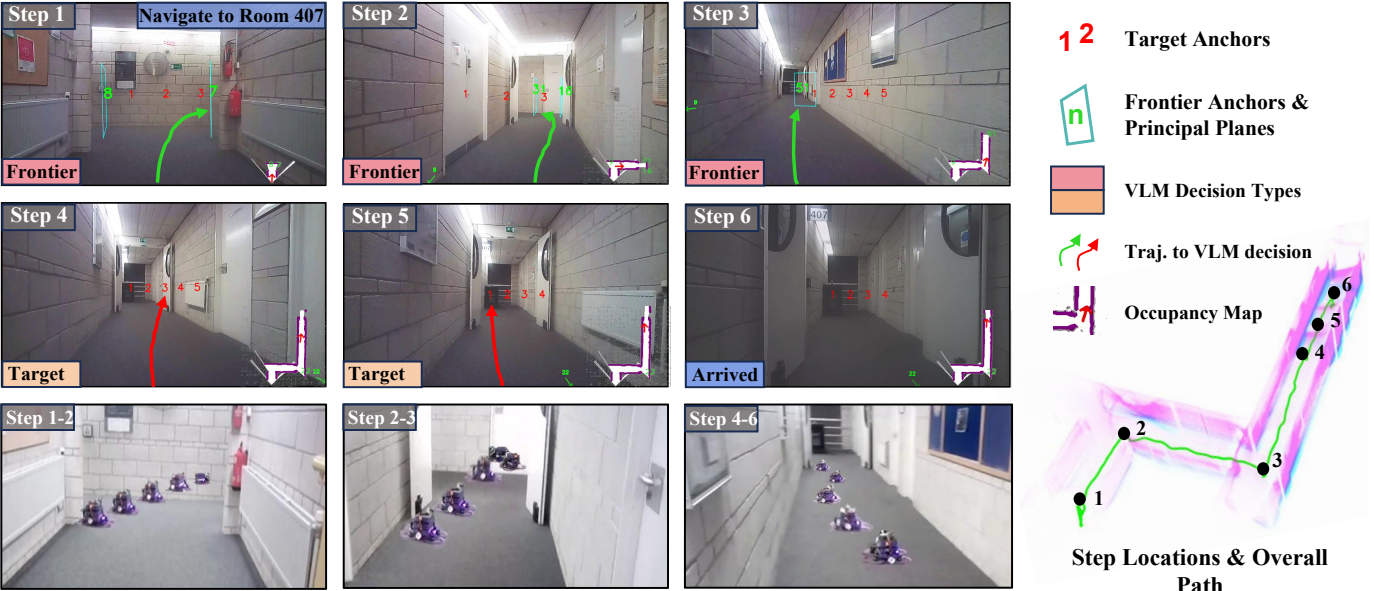


Fig. 6: Real-world Demonstration. We deployed our proposed method on real UAV, enabling autonomous navigation along an indoor corridor toward Room 407.

renewed reasoning. In contrast, Spatial frequently produces infeasible commands without geometric priors, leading to early termination. While our approach successfully finds the target in the Construction 3D environment, the Snowy 3D task remains highly challenging, as uniform visual cues hinder reasoning and the absence of yaw adjustment ultimately prevents success.

Overall, these results demonstrate that our method achieves average improvements of 25.7% (SR) and 17% (SPL) in 2.5D scenarios, and 29.5% (SR) and 18.5% (SPL) in 3D scenarios over the second-best method. These results demonstrate strong generalization across both short- and long-term tasks, with superior robustness and reliability compared to competing approaches.

#### D. Performance Across Different VLMs

Table II summarizes the performance of different VLMs in 2.5D and 3D scenarios. It shows that GPT-4o consistently outperforms other VLMs across both environments. In *Kilburn 2.5D*, it achieves efficient navigation with fewer prompts (5.67) while attaining the highest SR (0.67) and SPL (0.58). In *Warehouse 3D*, GPT-4o still yields the most balanced performance (Obs. = 0.80, SR = 0.57), but Sonnet4 surpasses it in SPL (0.32 vs. 0.18). Gemini2.5 and Qwen2.5 exhibit more stable prompt usage but considerably lower SR and SPL. These results suggest that GPT-4o excels in robustness and generalization, while Sonnet4 demonstrates relative efficiency in short-term planning.

#### E. Real-world Deployment

We deployed the proposed method on a customized UAV and successfully achieved autonomous navigation to **Room 407 in the Kilburn Building**. During the entire navigation process, the UAV interacted with **GPT-4o prompting for five**

**rounds**, resulting in a total trajectory length of 26.24m and a distance-to-goal (DtG) of 2.03m. The doorplate of Room 407 eventually appeared within FOV. As shown in Figure 6, the VLM selected **green frontier anchors** as navigation targets in Steps 1–3, indicating relatively low confidence in recognizing Room 407 at that stage. This allowed the UAV to pass around the corridor corner and effectively explore the unknown region through single-step decisions. In Steps 4–5, after entering the long corridor where Room 407 is located, the VLM switched to selecting **red target anchors** to approach the room.

## VIII. CONCLUSION

We presented a zero-shot VLM reasoning framework for adaptive UAV task-centric navigation. By combining multi-modal visual annotation with adaptive decision-making, our method maps high-level language outputs into executable UAV actions and switches to geometric strategies when semantic cues are weak. The proposed method outperforms baselines in prompting efficiency, SR, and SPL, and is further validated through deployment on a real UAV.

Despite promising results, the current approach only reasons in static conditions, missing valuable cues during motion. It also relies purely on geometric annotations, which may lead to target omission when semantic priors are absent. Additionally, the navigation memory lacks semantic structure, limiting alignment with human navigation logic. Future work will incorporate semantic priors and lightweight VLMs to leverage motion-aware cues for improved navigation performance.

## REFERENCES

- [1] Z. Li, H. Yu, Y. Ding, Y. Li, Y. He, and N. Akhtar, “Embodied intelligence for 3d understanding: A survey on 3d scene question answering,” *Information Fusion*, vol. 126, p. 103624, 2026. [Online]. Available: <https://www.sciencedirect.com/science/article/pii/S1566253525006967>

- [2] Y. Cui, L. Xie, Y. Zhao, J. Sun, and E. Yin, "Generating vision-language navigation instructions incorporated fine-grained alignment annotations," 2025. [Online]. Available: <https://arxiv.org/abs/2506.08566>
- [3] L. Ren, J. Dong, S. Liu, L. Zhang, and L. Wang, "Embodied intelligence toward future smart manufacturing in the era of ai foundation model," *IEEE/ASME Transactions on Mechatronics*, 2024.
- [4] P. Balatti, I. Ozdamar, D. Sirintuna, L. Fortini, M. Leonori, J. M. Gandarias, and A. Ajoudani, "Robot-assisted navigation for visually impaired through adaptive impedance and path planning," 2023. [Online]. Available: <https://arxiv.org/abs/2310.14705>
- [5] H. Song, J. Yu, J. Qiu, Z. Sun, K. Lang, Q. Luo, Y. Shen, and Y. Wang, "Multi-uav disaster environment coverage planning with limited-endurance," in *2022 International Conference on Robotics and Automation (ICRA)*. IEEE, 2022, pp. 10760–10766.
- [6] I. D. C. Caiza, A. Milas, M. A. M. Grova, F. J. Perez-Grau, and T. Petrovic, "Autonomous exploration of unknown 3d environments using a frontier-based collector strategy," 2023. [Online]. Available: <https://arxiv.org/abs/2311.12408>
- [7] B. Zhou, Y. Zhang, X. Chen, and S. Shen, "Fuel: Fast uav exploration using incremental frontier structure and hierarchical planning," 2020. [Online]. Available: <https://arxiv.org/abs/2010.11561>
- [8] Y. Zhang, X. Chen, C. Feng, B. Zhou, and S. Shen, "Falcon: Fast autonomous aerial exploration using coverage path guidance," 2025. [Online]. Available: <https://arxiv.org/abs/2407.00577>
- [9] O. Maksymets, V. Cartillier, A. Gokaslan, E. Wijmans, W. Galuba, S. Lee, and D. Batra, "Thda: Treasure hunt data augmentation for semantic navigation," in *Proceedings of the IEEE/CVF International Conference on Computer Vision*, 2021, pp. 15374–15383.
- [10] R. Ramrakhy, E. Undersander, D. Batra, and A. Das, "Habitat-web: Learning embodied object-search strategies from human demonstrations at scale," in *Proceedings of the IEEE/CVF conference on computer vision and pattern recognition*, 2022, pp. 5173–5183.
- [11] A. J. Sathyamoorthy, K. Weerakoon, M. Elnoor, A. Zore, B. Ichter, F. Xia, J. Tan, W. Yu, and D. Manocha, "Convoi: Context-aware navigation using vision language models in outdoor and indoor environments," 2024. [Online]. Available: <https://arxiv.org/abs/2403.15637>
- [12] N. Yokoyama, S. Ha, D. Batra, J. Wang, and B. Bucher, "Vlfm: Vision-language frontier maps for zero-shot semantic navigation," 2023. [Online]. Available: <https://arxiv.org/abs/2312.03275>
- [13] X. Wang, D. Yang, Z. Wang, H. Kwan, J. Chen, W. Wu, H. Li, Y. Liao, and S. Liu, "Towards realistic uav vision-language navigation: Platform, benchmark, and methodology," 2024. [Online]. Available: <https://arxiv.org/abs/2410.07087>
- [14] P. Gonzalez, A. Mora, S. Garrido, R. Barber, and L. Moreno, "Multi-lidar mapping for scene segmentation in indoor environments for mobile robots," *Sensors*, vol. 22, no. 10, 2022. [Online]. Available: <https://www.mdpi.com/1424-8220/22/10/3690>
- [15] Anthropic, "Introducing the next generation of claudie," 2024. [Online]. Available: <https://www.anthropic.com/news/claudie-3-family>
- [16] J. Roh, J. Kim, C. Park, and D. H. Shim, "Autonomous multi-floor and narrow indoor exploration using multi-criteria decision-making approach," in *2025 22nd International Conference on Ubiquitous Robots (UR)*. IEEE, 2025, pp. 260–267.
- [17] A. Rosinol, M. Abate, Y. Chang, and L. Carlone, "Kamera: an open-source library for real-time metric-semantic localization and mapping," in *2020 IEEE International Conference on Robotics and Automation (ICRA)*. IEEE, 2020, pp. 1689–1696.
- [18] S. Chen, T. Chabal, I. Laptev, and C. Schmid, "Object goal navigation with recursive implicit maps," in *2023 IEEE/RSJ International Conference on Intelligent Robots and Systems (IROS)*. IEEE, 2023, pp. 7089–7096.
- [19] M. Zhang, Y. Du, C. Wu, J. Zhou, Z. Qi, J. Ma, and B. Zhou, "Apexnav: An adaptive exploration strategy for zero-shot object navigation with target-centric semantic fusion," 2025. [Online]. Available: <https://arxiv.org/abs/2504.14478>
- [20] Y. Gao, C. Li, Z. You, J. Liu, Z. Li, P. Chen, Q. Chen, Z. Tang, L. Wang, P. Yang, Y. Tang, Y. Tang, S. Liang, S. Zhu, Z. Xiong, Y. Su, X. Ye, J. Li, Y. Ding, D. Wang, Z. Wang, B. Zhao, and X. Li, "Openfly: A comprehensive platform for aerial vision-language navigation," 2025. [Online]. Available: <https://arxiv.org/abs/2502.18041>
- [21] S. Nasiriany, F. Xia, W. Yu, T. Xiao, J. Liang, I. Dasgupta, A. Xie, D. Driess, A. Wahid, Z. Xu, Q. Vuong, T. Zhang, T.-W. E. Lee, K.-H. Lee, P. Xu, S. Kirmani, Y. Zhu, A. Zeng, K. Hausman, N. Heess, C. Finn, S. Levine, and B. Ichter, "Pivot: Iterative visual prompting elicits actionable knowledge for vlms," 2024. [Online]. Available: <https://arxiv.org/abs/2402.07872>
- [22] D. Goetting, H. G. Singh, and A. Loquercio, "End-to-end navigation with vision language models: Transforming spatial reasoning into question-answering," 2024. [Online]. Available: <https://arxiv.org/abs/2411.05755>
- [23] A. T. Kalai, O. Nachum, S. S. Vempala, and E. Zhang, "Why language models hallucinate," 2025. [Online]. Available: <https://arxiv.org/abs/2509.04664>
- [24] R. A. Newcombe, S. Izadi, O. Hilliges, D. Molyneaux, D. Kim, A. J. Davison, P. Kohi, J. Shotton, S. Hodges, and A. Fitzgibbon, "Kinectfusion: Real-time dense surface mapping and tracking," in *2011 10th IEEE international symposium on mixed and augmented reality*. Ieee, 2011, pp. 127–136.
- [25] X. Amatriain, "Prompt design and engineering: Introduction and advanced methods," 2024. [Online]. Available: <https://arxiv.org/abs/2401.14423>
- [26] S. Song, D. Kim, and S. Choi, "View path planning via online multiview stereo for 3-d modeling of large-scale structures," *IEEE Transactions on Robotics*, vol. 38, no. 1, pp. 372–390, 2021.
- [27] J. E. Bresenham, "Algorithm for computer control of a digital plotter," *IBM Systems Journal*, vol. 4, no. 1, pp. 25–30, 1965.
- [28] A. Hornung, K. M. Wurm, M. Bennewitz, C. Stachniss, and W. Burgard, "Octomap: An efficient probabilistic 3d mapping framework based on octrees," *Autonomous robots*, vol. 34, no. 3, pp. 189–206, 2013.
- [29] X. Zhou, Z. Wang, H. Ye, C. Xu, and F. Gao, "Ego-planner: An esdf-free gradient-based local planner for quadrotors," *IEEE Robotics and Automation Letters*, vol. 6, no. 2, pp. 478–485, 2020.
- [30] C. Group, D. Qigeng, L. Xuchen, and A. R. X. F.H., "Cu-astro," Video, Bilibili, September 2024, accessed: YYYY-MM-DD. [Online]. Available: <https://www.bilibili.com/video/BV1G6HmeqEZR/>
- [31] L. Technology, "Livox mid-360 lidar sensor," Available at: <https://www.livoxtech.com/mid-360>, 2024, accessed: 11 March 2025.
- [32] W. Xu, Y. Cai, D. He, J. Lin, and F. Zhang, "Fast-lio2: Fast direct lidar-inertial odometry," *arXiv preprint*, vol. 2107.06829, 2021. [Online]. Available: <https://arxiv.org/abs/2107.06829>
- [33] N. Corporation, "Nvidia jetson orin nx," <https://www.nvidia.com/en-us/autonomous-machines/embedded-systems/jetson-orin-nx/>, 2022, accessed: 2025-03-16.
- [34] M. Quigley, K. Conley, B. P. Gerkey, J. Faust, T. Foote, J. Leibs, R. Wheeler, and A. Y. Ng, "ROS: an open-source robot operating system," in *ICRA Workshop on Open Source Software*, vol. 3, no. 3.2, 2009, p. 5.
- [35] P. D. Team, "PX4 SITL (software-in-the-loop) simulator," <https://docs.px4.io/main/en/simulation/>, 2023, accessed: 2025-03-16.
- [36] N. Koenig and A. Howard, "Design and use paradigms for gazebo, an open-source multi-robot simulator," in *IEEE/RSJ International Conference on Intelligent Robots and Systems*. IEEE, 2004, pp. 2149–2154.
- [37] L.-S. D. Team, "livox\_laser\_simulation," [https://github.com/Livox-SDK/livox\\_laser\\_simulation](https://github.com/Livox-SDK/livox_laser_simulation), 2023, accessed: 2025-03-16.